MBS Endler et al.

Managing leading edges during assembly of the Wendelstein 7-X divertor

Preprint of Paper to be submitted for publication in
Plasma Physics and Controlled Fusion

Managing leading edges during assembly of the Wendelstein 7-X divertor

M. Endler, J. Fellinger, H. Hölbe, T. Sunn Pedersen,
S. Bozhenkov, J. Geiger, M. Grahl and W7-X Team
Max-Planck-Institut für Plasmaphysik, D-17491 Greifswald

19th November 2018

Abstract

Divertor target plates of magnetic confinement experiments are usually intersected by the magnetic field under a shallow angle. If steps are present in the target surface, the resulting leading edges will receive a strongly increased heat load as compared with the surrounding target surface. A very precise alignment of the target components is required to limit the height of leading edges in all magnetic configurations.

In preparation of the initial divertor operation phase of the Wendelstein 7-X (W7-X) stellarator, we combined a model calculating the thermal load pattern on the targets for each magnetic configuration with a time-dependent model for heat transport within the targets, with a model for carbon sublimation and with measurements of step heights between target components to estimate the carbon sublimation rates to be expected. In a few locations of the as-built and as-installed divertor, these were found to be critically high, such that a limitation of plasma performance might have resulted. By re-aligning one type of target component according to the results of our modelling, the expected carbon sublimation rates were strongly reduced to uncritical levels.

1   Introduction

Wendelstein 7-X (W7-X) is a large stellarator with superconducting coils, operated at the Greifswald site of the Max-Planck-Institut für Plasmaphysik (IPP) [1, 2]. In the long run,

it is planned to operate W7-X in steady-state discharges of up to 30 min with a continuous wave heating power of 10 MW. Under such conditions, a careful design and realisation of the water-cooled target plates for plasma-wall interaction is mandatory.

After a first operation phase with limiters on the inboard side of the plasma vessel wall [3, 4, 5], uncooled test divertor units (TDU) were installed for the second operation phase [6]. The TDU has the same geometry as the water-cooled High Heat Flux (HHF) divertor [7] to be used for long-pulse operation. The TDU serves to test divertor operation at an early phase without having to install the full cooling pipework inside the plasma vessel and in the periphery of the device. The power input in the TDU operation phase will be initially limited to 80 MJ per discharge (e. g., 8 MW ECRH for 10 s). The questions to be addressed during the TDU operation phase include the required accuracy of the alignment of the divertor units (1) absolutely in space and (2) relative to each other and (3) the tolerable height of leading edges, which in turn imposes accuracy requirements for the alignment of the adjacent divertor modules and target elements relative to each other.

However, we decided to reassess the potential impact of leading edges in the TDU operation phase, since

1. the alignment of the divertor support frames to the originally defined relative accuracy of 0.2 mm requires a significant amount of assembly time,

2. in contrast to later water-cooled HHF divertor operation, stationary target temperatures will not be reached during TDU operation (except, possibly, for an extended discharge length at low heating power),

3. only a limited number of magnetic configurations is envisaged for the TDU operation phase.

The aim of the reassessment was to relax the accuracy requirements for the TDU assembly but to avoid a situation where strong carbon sublimation from leading edges would limit the operation of W7-X.

In this paper, we discuss the modelling of the heat flux to leading edges of the target plates and the resulting carbon sublimation. In section 2, we shall explain the basic design of the W7-X divertor. In section 3, we shall introduce the accuracy requirements for steps within the target surface as originally defined for the HHF divertor and discuss the possibilities to relax these requirements for the TDU. Our approach to model the carbon sublimation rates at leading edges, to measure the as-built steps between different parts of the targets and to combine these into a prediction of carbon sublimation for different magnetic configurations is described in section 4. As a consequence, corrective

measures were taken, as discussed in section 5, and we present an overall assessment of the carbon sublimation to be expected from leading edges in the as-built TDU in section 6. Our conclusions are drawn in section 7.

2   The W7-X island divertor

In W7-X, the magnetic islands occuring naturally at magnetic surfaces with rational values of the rotational transform are used for divertor operation [8]. In such an island divertor, the islands are intersected by target plates. Due to the low magnetic shear in W7-X, rather long paths along the magnetic field within an island are achieved before a field line intersects a target plate (in the range 150–400 m) in spite of the small direct distance between the X points of the island chain and the target plates [9, 10].

Since the islands are arranged helically around the plasma axis, and the shape of the plasma cross-section changes for different toroidal positions, not every location is equally well suited to place target plates. Corresponding to the fivefold toroidal symmetry of the magnetic configuration (five "machine modules") and to the up-down flip symmetry (stellarator symmetry) within each machine module, there are 10 divertor units (DUs) of equal shape (see fig. 1). The basic building blocks of the targets are elongated target
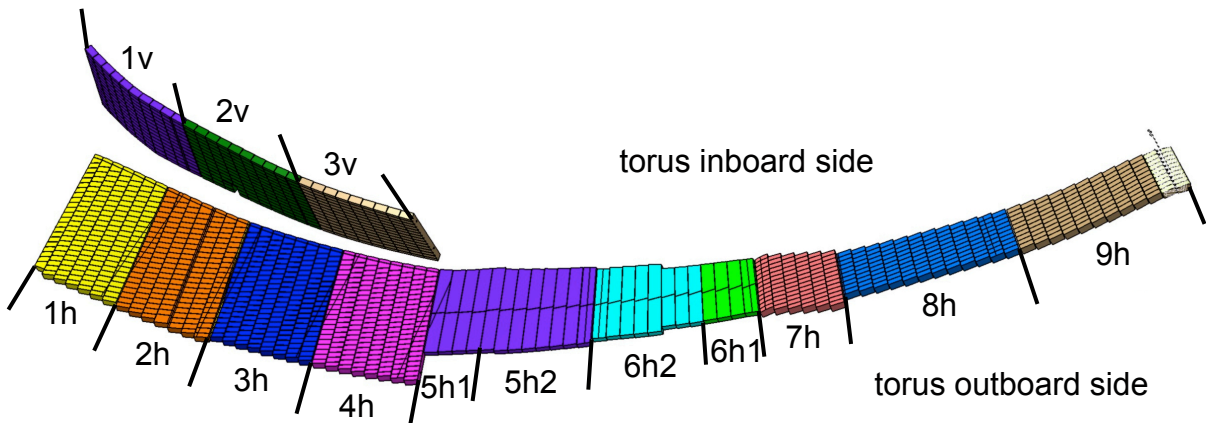
Figure 1: Design of a W7-X divertor unit. Each target module is identified by its short term and a different colour. There are 11 horizontal and 3 vertical target modules, each consisting of 4–10 target elements.

elements (TEs), 4–10 of which are grouped together into target modules (TMs). The TMs are pre-assembled outside the plasma vessel and are then integrated into their support frames inside the plasma vessel, using fitting elements. In each DU, there are 11 horizontal and 3 vertical TMs, identified by their short terms 1h to 9h and 1v to 3v in fig. 1.

The targets are three-dimensionally shaped in such a way that the thermal load does not exceed the design value of $10\,\mathrm{MW/m^2}$ locally (technological limit for the water-cooled TEs), and $1\,\mathrm{MW/m^2}$ for TMs 5h1 to 6h1, using a simple field line diffusion model (as described, e.g., in [11]) with an assumed diffusion coefficient of $1\,\mathrm{m^2/s}$, for any of nine reference magnetic vacuum configurations. The resulting targets intersect the magnetic field at angles of $1°$–$3°$ in those regions where the heat flux along the magnetic field is largest, thus limiting the thermal load to the targets as required.

Under the aforementioned assumptions, the maximal heat load onto surfaces oriented perpendicular to the magnetic field (such as leading edges) is expected to be of order $200\,\mathrm{MW/m^2}$. Therefore, the height of leading edges must be minimised. The locations of the regions of highest thermal load (strike lines) on the targets in reality may deviate from the modelling due to deviations of the magnetic field from the underlying vacuum configurations (finite-β effects, additional driven plasma currents, use of different magnetic configurations), but also due to particle drifts which are not taken into account in the model. Therefore, the design of the targets was chosen in a way to minimise leading edges between TEs everywhere on the target surface by introducing steps and slight inclinations at gaps, such that leading edges are shadowed by the adjacent TE.

Due to technical boundary conditions, there exist gaps of up to $7\,\mathrm{mm}$ between TMs in some locations, and there is a poloidal watershed in some areas of the targets (see fig. 2 — the watershed is defined as the line where the angle of incidence of the magnetic field on the target surface changes sign, here between the torus outboard and inboard sides of the targets).

3   Requirements on the relative accuracy during divertor assembly

If there is a gap between TEs crossing the watershed, the potential leading edge will change side between the two TEs at the watershed, and the TEs must be inclined relative to each other in order to achieve shadowing on both sides of the watershed (see fig. 3). However, the position of the watershed changes by several centimetres between magnetic configurations, such that a compromise for the design of the TEs had to be found, which was a maximum leading edge of nominally $0.2\,\mathrm{mm}$ along a short section of the gap and a required relative positioning accuracy of $0.2\,\mathrm{mm}$ between adjacent TEs, resulting in a maximum leading edge of $0.4\,\mathrm{mm}$.

The components were designed accordingly. The TEs were assembled into TMs with high precision outside the plasma vessel. Support frames were integrated into the plasma vessel, where they should be adjusted relative to each other with the required accuracy.
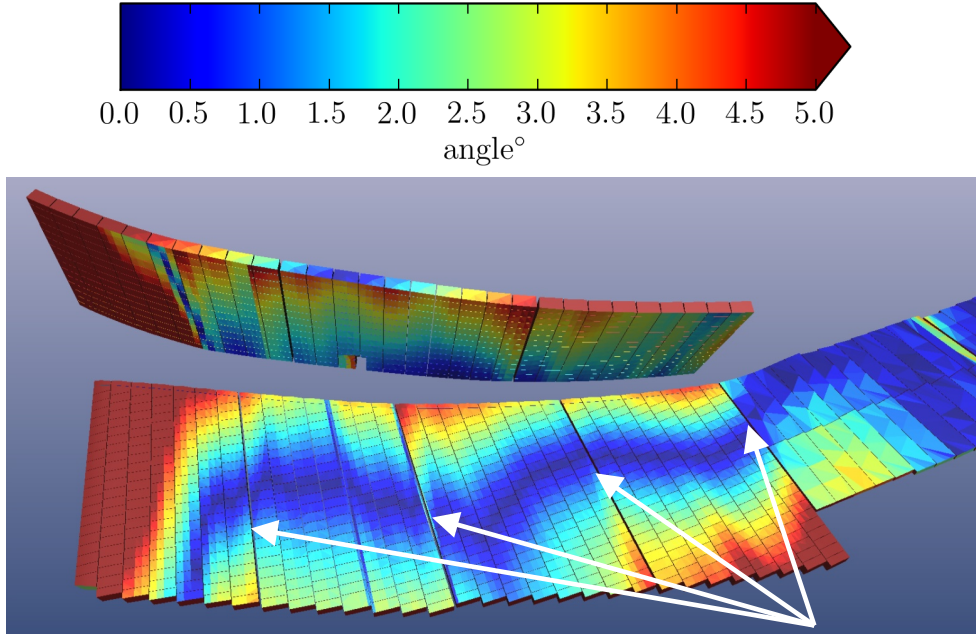
Figure 2: Incident angle of the magnetic field on part of the targets. The larger gaps of (5 ± 1.5) mm between adjacent target elements are indicated by arrows. The direction of incidence is not shown, but the poloidal "watershed" with an angle of incidence of 0 is clearly visible along most of the horizontal targets. The direction of incidence changes sign when crossing the poloidal watershed (see fig. 3).

The TMs should then be attached to the frames with fitting elements, such that adjacent TMs would have the required relative positioning accuracy by design.

As discussed in section 1, we decided to reassess the potential impact of leading edges for the TDU operation phase in order to relax the accuracy requirements for assembly.

Rather than avoiding leading edges with an effective height above 0.2 mm everywhere on the target surface, we focused on the locations of the strike lines (according to the field line diffusion model) and on those magnetic configurations likely to be operated at high power in the TDU phase. We would allow for larger tolerances of the targets, compatible with the assembly time schedule, but would measure the resulting step height along the gaps between TEs. We would estimate the expected carbon sublimation rate due to the as-built steps for the specified magnetic configurations and would re-align the targets if the estimated carbon sublimation was so large that radiation collapses would likely limit the operation of W7-X.

The original strategy, to use the same tolerance scheme for the TDU assembly as
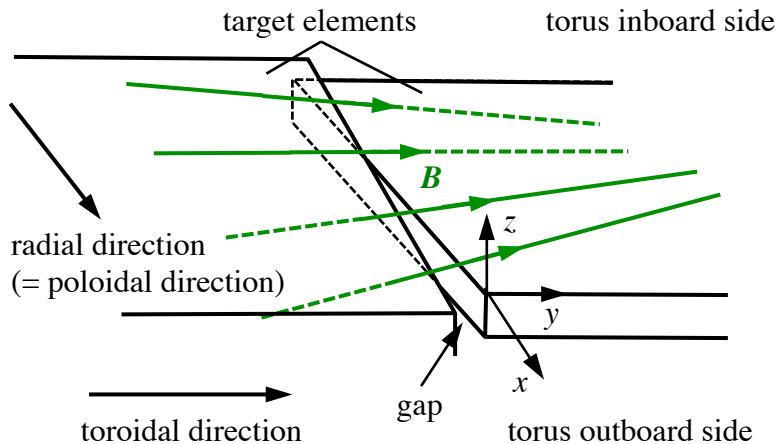
Figure 3: Schematic view of the relative inclination of two target elements with a gap which might cause leading edges to be exposed to heat flux from the plasma along the magnetic field lines. In this case, the direction of incidence of the magnetic field reverses along the gap, and the two target elements are inclined in such a way that the leading edge is always shadowed by the adjacent target element. Since the point of field inclination reversal shifts poloidally for different magnetic configurations and since the target elements are positioned within a given accuracy, the shadowing will not be perfect for all configurations.

required for the HHF divertor, was in this respect modified.

4 Approach to assessment of the impact of leading edges

4.1 Model for carbon sublimation at leading edges

The goal for the positioning of the TDUs was to avoid steps between adjacent TEs which might cause such high carbon sublimation rates due to plasma hitting leading edges that operation in the TDU phase would be severely limited. We use a carbon sublimation rate

$$e(T) = A\,T^{3.25}\,\exp\left(\frac{-W}{k_\mathrm{B}T}\right), \tag{1}$$

which was given in [12] for temperatures up to $\sim 2000°\,$C. Here, the constant $A = 2.5 \times 10^{24}\,\mathrm{K}^{-3.25}\,\mathrm{m}^{-2}\,\mathrm{s}^{-1}$, T is the surface temperature, and $W = 7.44\,\mathrm{eV}$ is the sublimation heat of carbon. The authors of [12] used this formula as a good analytic approximation describing data presented in [13]. In that work, the different vapor pressures and sticking

6

coefficients of carbon clusters were taken into account. In our model, significantly higher target temperatures result at leading edges. We are nevertheless using the above formula for $e(T)$, since in the high temperature range sublimation dominates the energy sinks, such that the sublimation rate is directly determined by the local incident power and the sublimation heat of $7.44\,\text{eV}$ per carbon atom.

In a Finite Element Method (FEM) model of a leading edge (see fig. 4), the local tem-
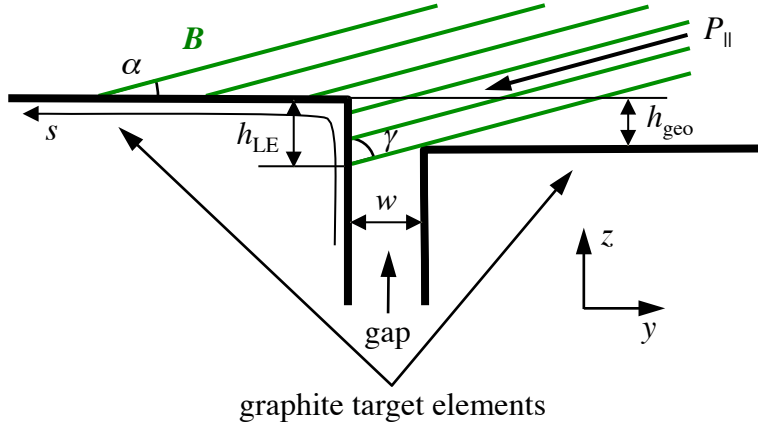

Figure 4: *Geometry of FEM model to calculate the carbon sublimation rate at a leading edge of height h_{LE} (yz plane of fig. 3). Two effects can contribute to h_{LE}, (1) a step height h_{geo} between two adjacent target elements, which is independent of the magnetic configuration, and (2) a gap of width w between the target elements in a magnetic field $\boldsymbol{B}$ with small angle of incidence to the surface of the target element. Depending on the direction of incidence of the magnetic field, h_{geo} may increase (as shown here) or decrease the leading edge due to the gap. For the FEM model, the target elements are assumed to be infinitely long in the x direction (see text). The time evolution of the surface temperature along the s coordinate, which runs first in z direction, then in y direction, is calculated after switching on the incident convective power density $P_{\parallel}$ along the magnetic field. The angle of incidence of $\boldsymbol{B}$ onto the leading edge surface is defined as $\gamma = \arcsin|\boldsymbol{B}\cdot\boldsymbol{y}|$, which accounts for an x component of $\boldsymbol{B}$.*

perature is obtained by balancing the incident power onto the target surface P at a leading edge with thermal radiation from the unshielded surface of the TE, heat conduction into the bulk graphite, and cooling by carbon sublimation. The resulting temperature field $T(t, P, h_{\text{LE}}, s)$ is used to calculate the sublimation rate $e_{\text{int}}(t, P, h_{\text{LE}})$ per unit length of the leading edge (along the x coordinate of fig. 3), where t is the time from the start of the discharge, h_{LE} is the height of the leading edge, taking into account the step height h_{geo}, the gap width w and the incident angle of the magnetic field, and s is the posi-

tion along the two faces of the TE, perpendicular to the length of the gap (see fig. 4). Thermionic emission of electrons and effects of plasma physics like impurity radiation, or of plasma-surface interaction like modification of the sheath transmission factor [12], are not considered. Details of the model are explained in the appendix.

The FEM model is used to create a table of $\ln(e_{\text{int}}(t, P, h_{\text{LE}}))$ values for t in the range 0 to 40 s, P in the range 10 MW to 230 MW, and h_{LE} in the range 0 mm to 3 mm. This table can then be used to quickly compute, by appropriate interpolation, the e_{int} values for any given set of (t, P, h_{LE}) values along the gaps between TMs.

By integrating e_{int} along a gap (along x), where P and h_{LE} will vary along the gap, a total sublimation rate $e_{\text{tot}}(t)$ for a specific gap and a specific magnetic configuration is calculated. Although the variation of P and h_{LE} would require a three-dimensional model, where heat conduction along x is taken into account, we note that the bulk graphite temperature varies on a scale of few millimetres in the yz plane (see fig. 13), whereas the variation along x is on a scale of centimetres. The three-dimensional shaping of the targets also implies that, in general, the gap between two TEs is not straight. This is on a still larger scale and is accounted for in the calculation of step heights and angles of incidence of the magnetic field but neglected in figs. 3 and 4. Altogether, this justifies the use of a two-dimensional heat conduction model with the present level of accuracy of the overall model.

4.2   Calculation of incident power

A simple estimate of the local power density to a target surface is provided by the "field line diffusion" model: Magnetic field line tracing is started at arbitrary points slightly inside the last closed magnetic flux surface, and after some "free path" length, a random step perpendicular to the magnetic field is added. This corresponds to test particles moving parallel to the magnetic field and undergoing a diffusion perpendicular to the magnetic field [11]. The parameters of this process are chosen to reflect the ratio of parallel to perpendicular transport in the plasma edge. In the end, all the tracing paths will intersect some wall component. The density of hit points on the target surface is then a measure for the power density in this location for the underlying magnetic configuration. The incident power density can also be computed by more sophisticated models like the EMC3/Eirene code [14], which is, however, significantly more computationally expensive. Both approaches were used, but most calculations were performed with field line diffusion.

In order to obtain a good spatial resolution along the gaps between TEs (in the x direction), we subdivided the target surface into pieces with a length of 5 mm along x and 40 mm along y. Achieving good statistics then requires the tracing of $\mathcal{O}(10^6)$ test particles.

In most areas, the magnetic field intersects the target surface under a small angle α. The incident power density parallel to the magnetic field $P_\parallel$ is therefore larger by a factor of $1/\sin\alpha$ than the power density P_{surf} to the surrounding target surface. A leading edge hit under an angle γ is then exposed to a power density

$$P = P_{\text{surf}} \frac{\sin\gamma}{\sin\alpha}, \tag{2}$$

and γ is typically much larger than α. Nevertheless, since the loaded area of a leading edge is very small for steps on the order of $0.2\,\text{mm}$, only a small number of test particles hits these faces directly. An even higher starting number of test particles than $\mathcal{O}(10^6)$ would be required to achieve good statistics for these faces. P or $P_\parallel$ is therefore not directly available in the field line diffusion code, in contrast to P_{surf}. In addition, the step height between adjacent divertor modules is varied during the optimisation procedure (see section 5), which would require a multiple repetition of the field line diffusion calculation for different step heights.

In our implementation, we therefore use field line diffusion or EMC3/Eirene to calculate P_{surf} and obtain the power density P to the leading edge by use of eq. (2). The local power density P_{surf} as a function of position x along the gap remains independent of the step height and only depends on the choices of gap and magnetic configuration. The total sublimation rate along the gap $e_{\text{tot}}(t)$ can then quickly be evaluated for different step heights h_{LE}, as outlined at the end of section 4.1. What is dependent on h_{LE} is the potential shadowing of the surface of the adjacent TEs. However, since the step heights considered remain small enough, their variation does not cause shadowing at a neighbouring gap, and we are only using the heat loads at the gaps in our analysis.

In some target areas, the surface is almost parallel to the magnetic field. Without transport perpendicular to the magnetic field, these areas would see no heat load at all. $P_\parallel = P_{\text{surf}}/\sin\alpha$ assumes that there is *no* perpendicular transport and must therefore be corrected to avoid unphysical peak values in P: If for a given gap the maximum of $P_{\text{surf}}/\sin\alpha$ is located in an interval where α is smaller than the ratio of the perpendicular to the parallel transport as used in the field line diffusion model ($\equiv \alpha_{\text{lim}}$), then the peak value of $P_\parallel$ is replaced by the average of the two $P_\parallel$ values just outside this interval. This procedure is repeated until the maximum of $P_\parallel$ is no longer located in an interval with $\alpha < \alpha_{\text{lim}}$. For our purpose to calculate the thermal load to only one leading edge at a time, this procedure yields satisfactory results.

As examples, we show in fig. 5 surface loads P_{surf} and resulting loads P on leading edges at the gap between two modules of the horizontal target for two different magnetic configurations ("scraper element mimic configurations" for a toroidal plasma current of 0 and of $43\,\text{kA}$, see [15]).
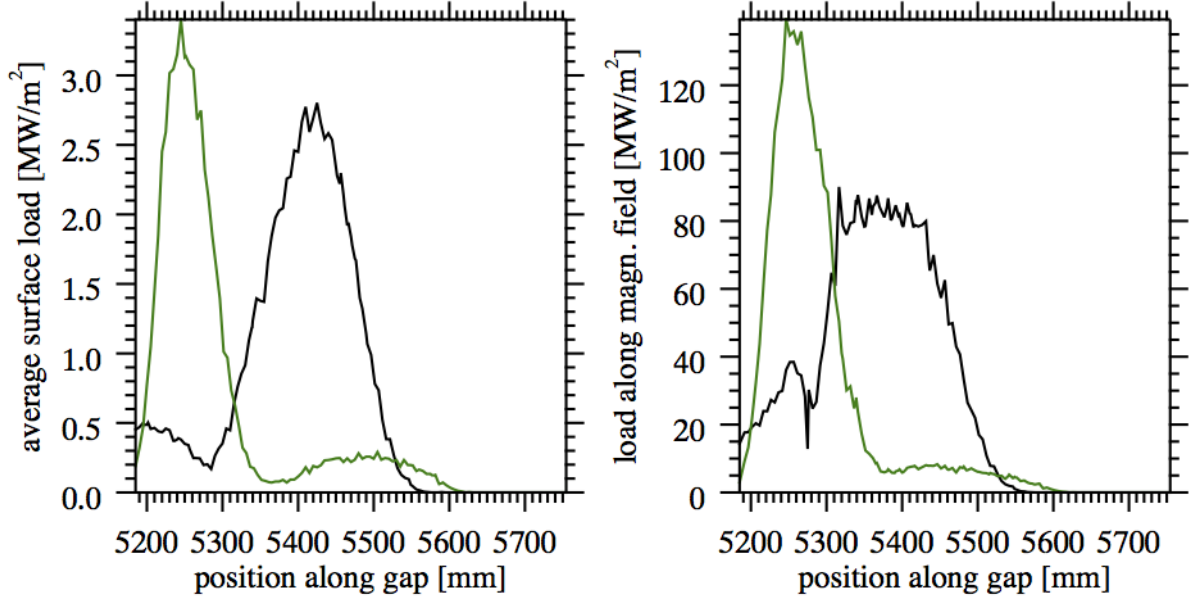
Figure 5: Left: surface power loads P_{surf} to the target surfaces adjacent to the gap between target modules 3h and 4h, as calculated in a field line diffusion model, for two magnetic configurations ("scraper element mimic configuration" for toroidal plasma currents of 0 (black) and 43 kA (green)); right: resulting power loads P to a leading edge. The abscissa coordinate is the length along the gap (x of fig. 3), with the major radius of the inboard end of the gap as an offset.

4.3 As-built steps between target elements

After installation of each test divertor unit in the W7-X plasma vessel, the step height h_{geo} (see fig. 4) was measured with a dial gauge at 3–4 positions along the gap between any two adjacent TMs. The deviation of the measured steps from the design values Δh_{geo} was then interpolated with a quadratic function (for 3 measurement positions along the gap) or cubic spline (for 4 measurement positions along the gap) to obtain the as-built $h_{geo, \text{as-built}} = h_{geo, \text{CAD}} + \Delta h_{geo, \text{interpol.}}$ along the gap. An example is shown in fig. 6.

4.4 Calculation of temperature and sublimation rates

The effective height of the leading edge h_{LE} (see fig. 4) can now be calculated for a given magnetic configuration from $h_{geo, \text{as-built}}$ and from the magnetic field vector and the surface normal vector for each point along the target edge (see fig. 7 for an example).

Likewise, for each point along the target edge the incident power density P_{LE} to the
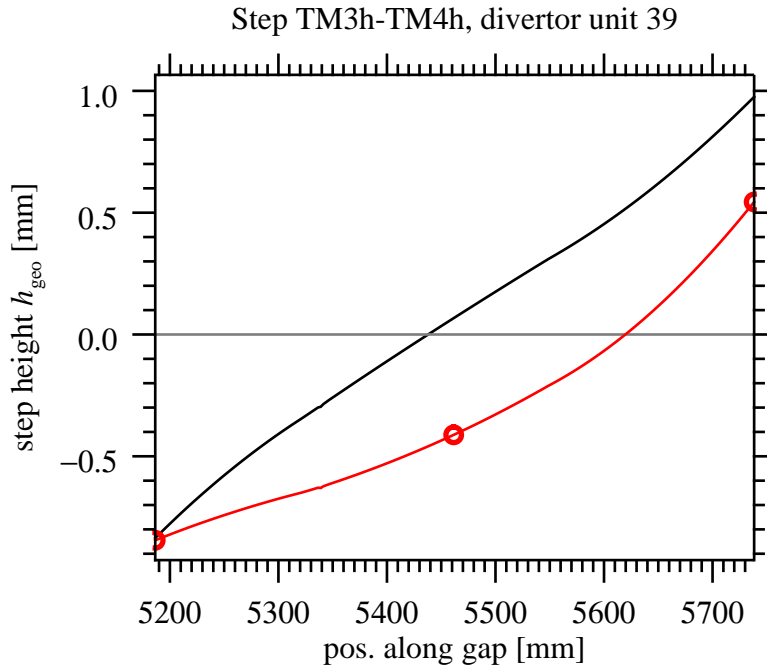
10

Figure 6: Step height h_{geo} (see fig. 4) between the adjacent target modules 3h and 4h in divertor unit 39 (height of target module 4h edge above target module 3h edge) — design (black) versus as-built (red). The three measurements along the gap are marked by circles. According to the design, the edges of the two target modules are tilted relative to each other since the direction of incidence of the magnetic field changes sign along the gap, as shown in fig. 3.

leading edge can be calculated for each magnetic configuration from $P_\parallel$ of section 4.2 and from the magnetic field vector and the normal vector on the face of the leading edge (see fig. 8 for an example, together with the resulting maximum temperatures).

The table of $\ln(e_{int}(t, P, h_{LE}))$ values of section 4.1 can now be used to bi-linearly interpolate $\ln e_{int}$ for each point along the gap to the corresponding (P_{LE}, h_{LE}) values and to obtain e_{int} by exponentiation for each tabulated time t (see fig. 9, left panel, for an example). Finally $e_{tot}(t)$ for this gap can be calculated (see fig. 9, right panel).

5 Optimising the steps between divertor modules

In the framework of our model, we calculated sublimation rates for the as-built state of all gaps between TMs in all ten test divertor units of W7-X, as described in section 4.
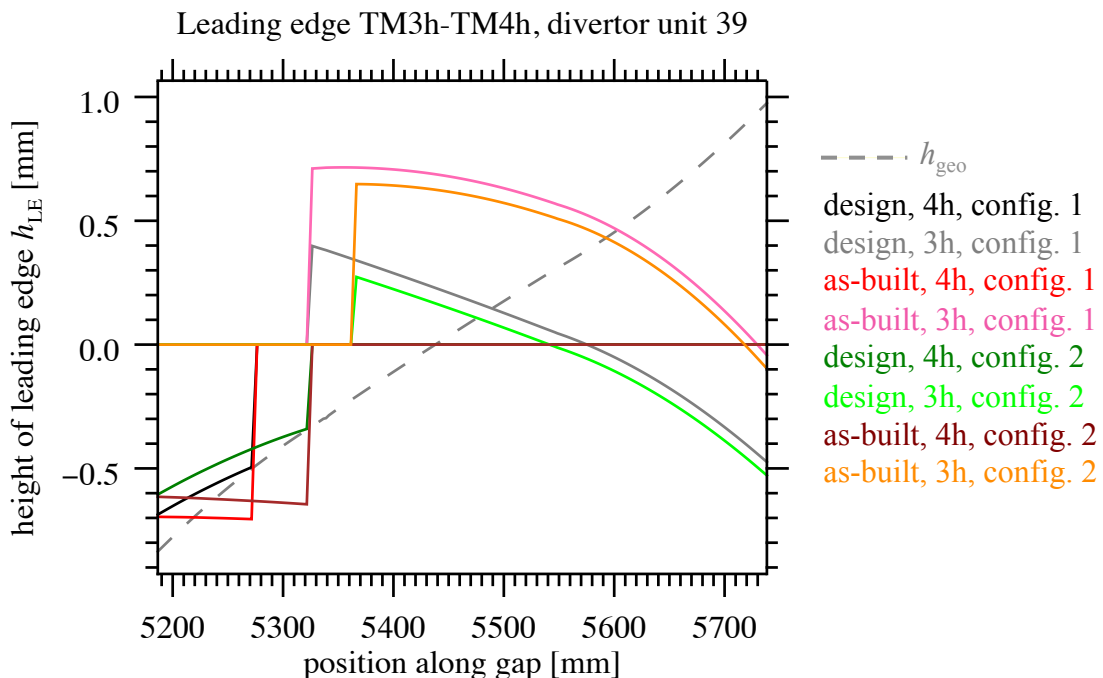
11

Figure 7: Height of leading edges h_{LE} (see fig. 4) between the adjacent target modules 3h and 4h in divertor unit 39, comparison between design and as-built state, example for two magnetic configurations: "scraper element mimic configurations" (see section 4.2) for toroidal plasma currents of 0 (config. 1) and 43 kA (config. 2). h_{LE} is calculated from h_{geo} (shown in dashed grey, compare fig. 6), using the local inclination angle of the magnetic field. h_{LE} is shown at target modules 4h and 3h. h_{LE} is set to 0 where the field lines are inclined in such a sense that the corresponding target edge is not exposed. Negative values indicate that this edge would be exposed, but is in the shadow of the opposite target module (see fig. 3). The position of reversal of the sense of incidence (poloidal watershed) is different for the two magnetic configurations. It does not depend on the step height and is therefore located at the same x position in the design and the as-built cases for the same magnetic configuration.

We did this for a number of magnetic configurations, which were considered relevant for the TDU operation phase.

Our criterion was to avoid a situation where the operation of W7-X would be limited by strong carbon sublimation from leading edges. With a plasma volume of roughly $30\,m^3$ and an assumed plasma density of at least $2 \times 10^{19}\,m^{-3}$, we obtain an overall particle content of 6×10^{20}. Therefore, the plasma should certainly not contain more than 10^{20}
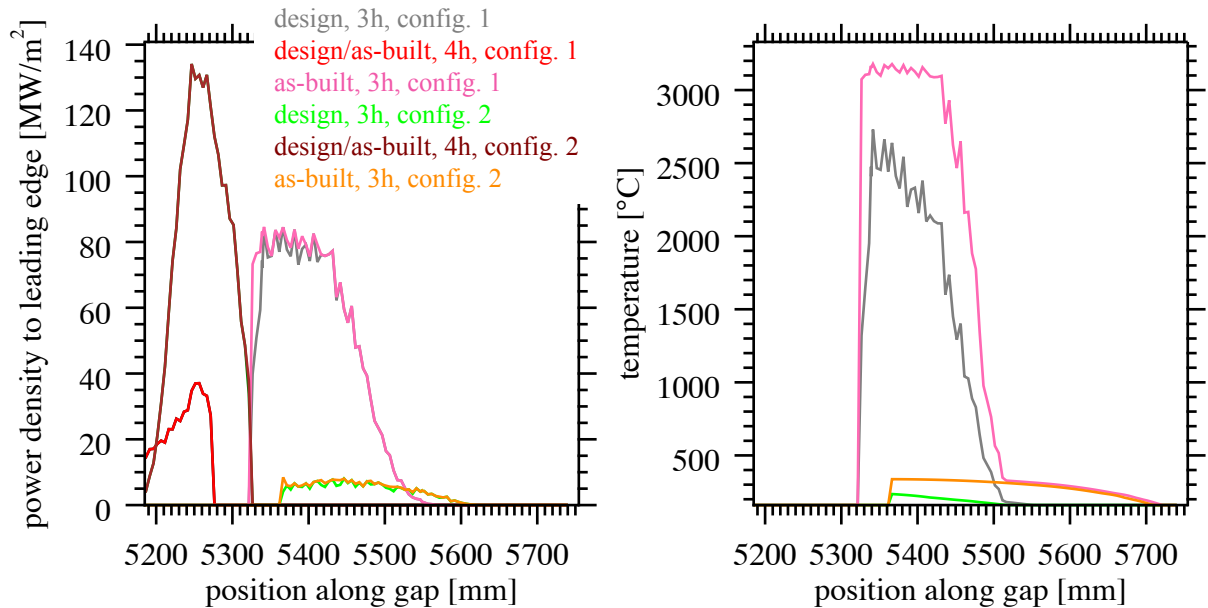
Figure 8: Incident power P_{LE} to the (potential) leading edges between the adjacent target modules 3h and 4h in divertor unit 39 (left) and resulting maximum temperatures after 8 s (right). The values are shown for the two "scraper element mimic configurations" for toroidal plasma currents of 0 (config. 1) and 43 kA (config. 2). The colours are the same as in fig. 7. P_{LE} is shown even where the corresponding leading edge is shadowed by the opposite target module, but set to 0 where the sense of incidence does not expose the edge. The temperatures are of course only elevated where an edge is exposed to the power load. The temperature differences between the two magnetic configurations as well as the differences between design case and as-built state (which in this case is unfavourably misaligned) are clearly visible.

carbon ions, corresponding to 2×10^{-3} g. We choose a sublimation rate of 2×10^{-3} g/s as a critical threshold. Considering the uncertainties of modelling, 10^{-4} g/s will be regarded as a second threshold.

As mentioned in section 3, a precise alignment of most of the TMs would require a significant amount of assembly time. However, one type of TM can be re-aligned within its divertor frame without major time effort. This type of TM (TM5h1) happens to have a critical gap toward TM4h, where a large carbon sublimation rate is likely in case of misalignment. Our compromise for the assembly strategy therefore was to plan for a re-alignment of TM5h1 in all ten DUs, whereas we would monitor all other gaps between TMs and only take action, if our model would indicate a particularly high sublimation
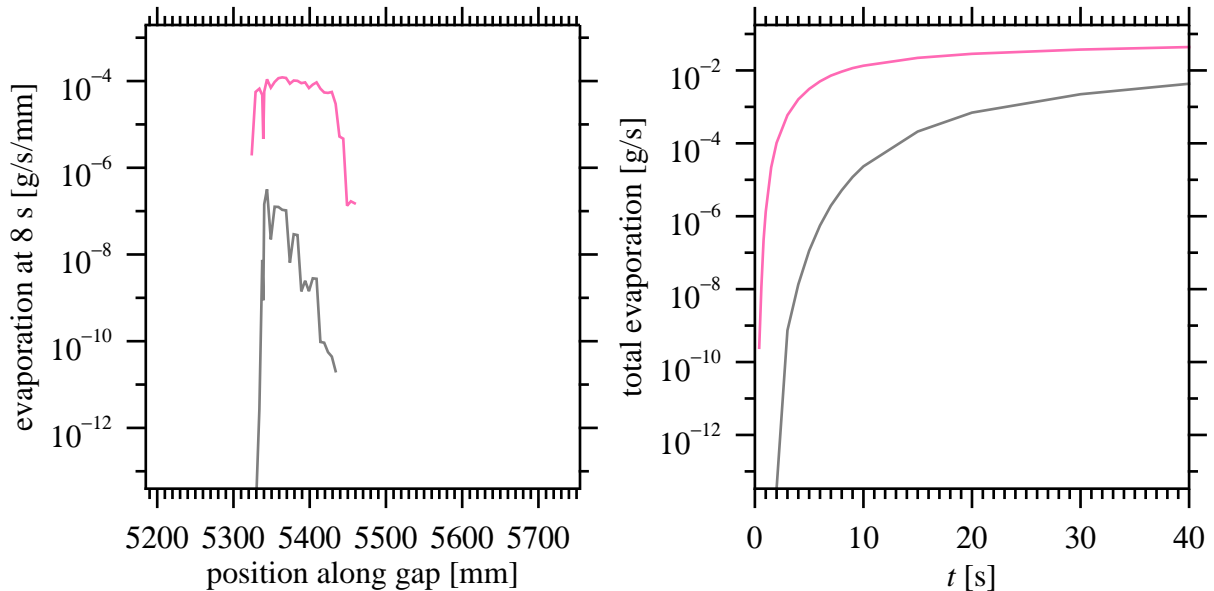
Figure 9: Left: sublimation rates e_{int} after 8 s, corresponding to the temperatures in fig. 8, right panel. Of the two magnetic configurations treated in figs. 7 and 8, only in the "scraper element mimic configuration" for toroidal plasma current 0 and only at the leading edge at target module 3h the temperatures are high enough to yield significant carbon sublimation after 8 s. Whereas in the CAD alignment (grey curves), the sublimation rate is still tolerable at this time of the discharge, it becomes three orders of magnitude larger for the as-built alignment (pink curves). Right: Time evolution of the total sublimation rate e_{tot}, integrated along the entire gap.

rate at such a location.

Once the as-built step heights between the TMs 4h, 5h1 and 5h2 had been measured in a DU, the necessary shifts were calculated. TM5h1 is positioned into the divertor frame by means of two fitted brackets and one fitted bush. For the new alignment, TM5h1 was removed, new brackets and a new bush were manufactured to the newly calculated measures, the TM was reinstalled, and the step heights were measured again. A typical accuracy of ~ 0.2 mm was thus achieved.

The re-alignment changes the step heights at the gaps between TM4h and TM5h1, and between TM5h1 and TM5h2. In order to find the optimum alignment of TM5h1, the step heights at the inboard end and at the outboard end of the gap are represented by a pair of values (h_1, h_2), which are then varied. For each realisation of (h_1, h_2), the new total sublimation rates after 8 s at the two gaps in question are calculated for a number

of magnetic configurations considered relevant for the test divertor operation phase. This includes several of the vacuum reference configurations originally defined during the design of the W7-X device [16], but also finite-β configurations based on VMEC [17] simulations, and special configurations for the investigation of the limits of the divertor. Depending on their "importance", each configuration was assigned a weight, and the calculated sublimation rates are multiplied by these weights (with the sum of the weights being unity) and then summed up. This sum is minimised by varying the parameters (h_1, h_2). In fact, we perform a stochastic optimisation, i.e., we optimise the sublimation rate for Gauss distributions of shifts around each pair of nominal (h_1, h_2) values, with standard deviations of 0.2 mm. By this procedure we avoid to choose a narrow minimum which will most probably not be realised due to the finite accuracy of the re-alignment.

In figs. 10–11, the effect of the re-alignment is illustrated for the case of divertor unit
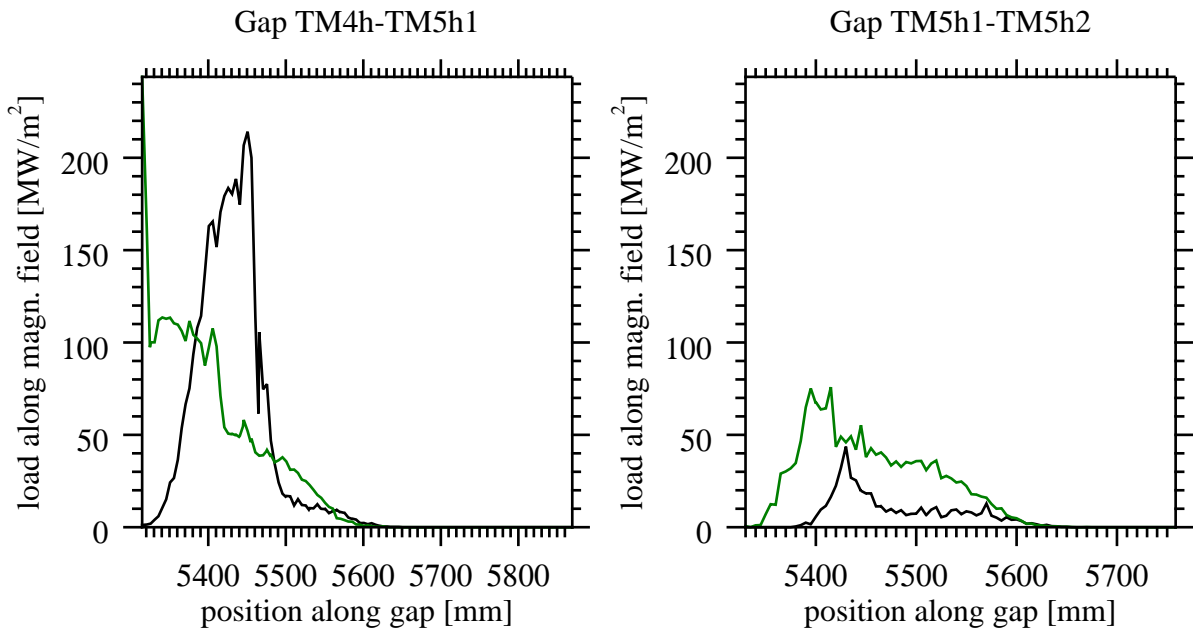

Figure 10: *Power loads P to leading edges at the gaps between target modules 4h and 5h1 (left) and between target modules 5h1 and 5h2 (right) for two magnetic configurations ("standard configuration" (black) and "scraper element mimic configuration" for a toroidal plasma current of 22 kA (green), see [15]). The abscissa coordinate is the length along the gap (x coordinate of fig. 3), starting at the major radius of the inboard end of the gap.*

48, with a comparison of the original as-built state and the new optimised target values for the step heights. In this divertor unit, TM 5h1 was very unfavourably aligned, which
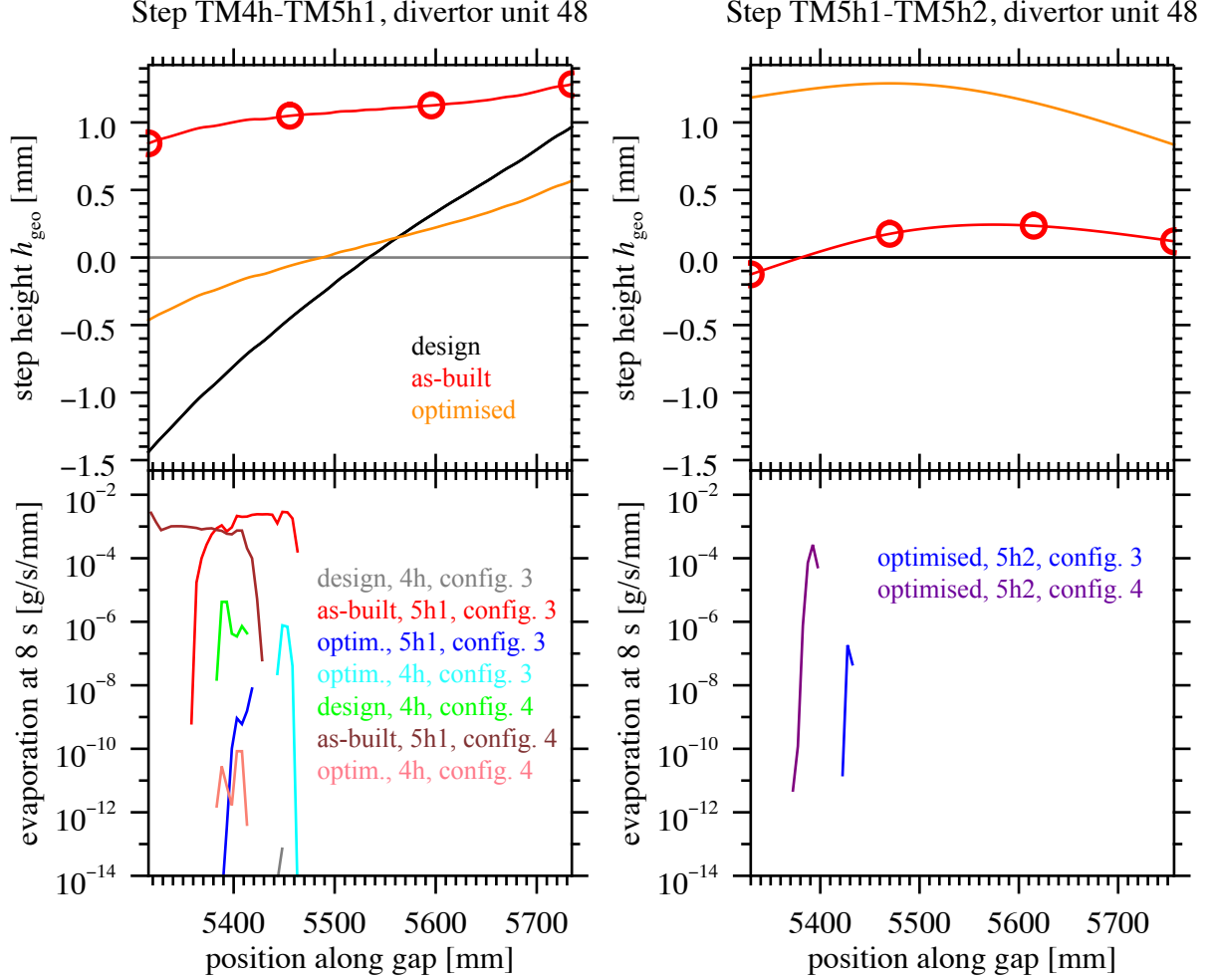
Figure 11: Top: Step height h_{geo} (see fig. 4) between the adjacent target modules 4h and 5h1 (left) and between 5h1 and 5h2 (right) in divertor unit 48 (height of target module 5h1 (5h2) edge above target module 4h (5h1) edge) — design versus as-built and after optimised alignment. The four measurements along the gaps are marked by circles. Bottom: sublimation rates e_{int} after 8 s for the three different alignments of target module 5h1. The "standard configuration" (config. 3, black in fig. 10) is compared with the "scraper element mimic configuration" for a toroidal plasma current of 22 kA (config. 4, green in fig. 10). For a discussion, see text.

would have resulted in a leading edge of $\sim 1\,\text{mm}$ at the location of the strike line (top left in fig. 11, red line, and left in fig. 10), leading to considerable carbon sublimation in

both magnetic configurations shown here as examples (red and brown lines bottom left in fig. 11). The optimisation pushes the step height back toward the CAD alignment at the 4h-5h1 gap (top left in fig. 11, orange line) at the cost of a $\sim 1\,\mathrm{mm}$ leading edge at the 5h1-5h2 gap (top right in fig. 11). At the 5h1-5h2 gap, however, the power flux to the divertor is significantly lower (right in fig. 10), such that the carbon sublimation rates for the re-aligned placement remain moderate (bottom right in fig. 11). The sum of the weighted averages of the sublimation rate from both gaps would in this case be reduced from $0.27\,\mathrm{g/s}$ (initial installation) to $6.7 \times 10^{-4}\,\mathrm{g/s}$ (re-aligned).

6 Results of test divertor assembly

The resulting carbon sublimation rates from our model for each gap between TMs and for the steps between certain TEs are summarised in fig. 12. The value for each gap is the weighted average of the results for different magnetic configurations, as defined in section 5. In many cases, only one or two magnetic configurations contribute significantly, such that the values for such a configuration could be higher by a factor ~ 10.

We note that the critical thresholds $10^{-4}\,\mathrm{g/s}$ and $2 \times 10^{-3}\,\mathrm{g/s}$ introduced in section 5 (grey horizontal lines in fig. 12) are already reached or exceeded at several gaps. The limit of $2 \times 10^{-3}\,\mathrm{g/s}$ was only exceeded at gap no. 6, which is between the TMs 4h and 5h1, before the re-alignment described in section 5 (full symbols), and at gap no. 3 in one case (full red square). The latter case concerned one TE with inlays for the investigation of plasma-wall interactions, which was also re-aligned. In all cases, the modelled sublimation rates after the re-alignment (open symbols) did not exceed the threshold of $2 \times 10^{-3}\,\mathrm{g/s}$.

7 Conclusions

We combined a model for heat flux onto the divertor target plates (based on field line diffusion), a model calculating the resulting heat flux to a leading edge (depending on the local angle of incidence of the magnetic field), a thermal model of time-dependent heat conduction into the target surface, and a model for the carbon sublimation rate (depending on the surface temperature) with the measurement of the as-built step height between adjacent parts of the target surface.

A number of effects is not included in our model, such as a reduction of the heat flux toward the target due to plasma radiation/detachment, a modification of the heat flux due to sheath effects (secondary electron emission/change of sheath transmission factor), as discussed, e. g., in [12], arcing, or sputtering. The anomalous transport, which is dominant in the edge plasma and scrape-off layer (SOL) and determines, together with
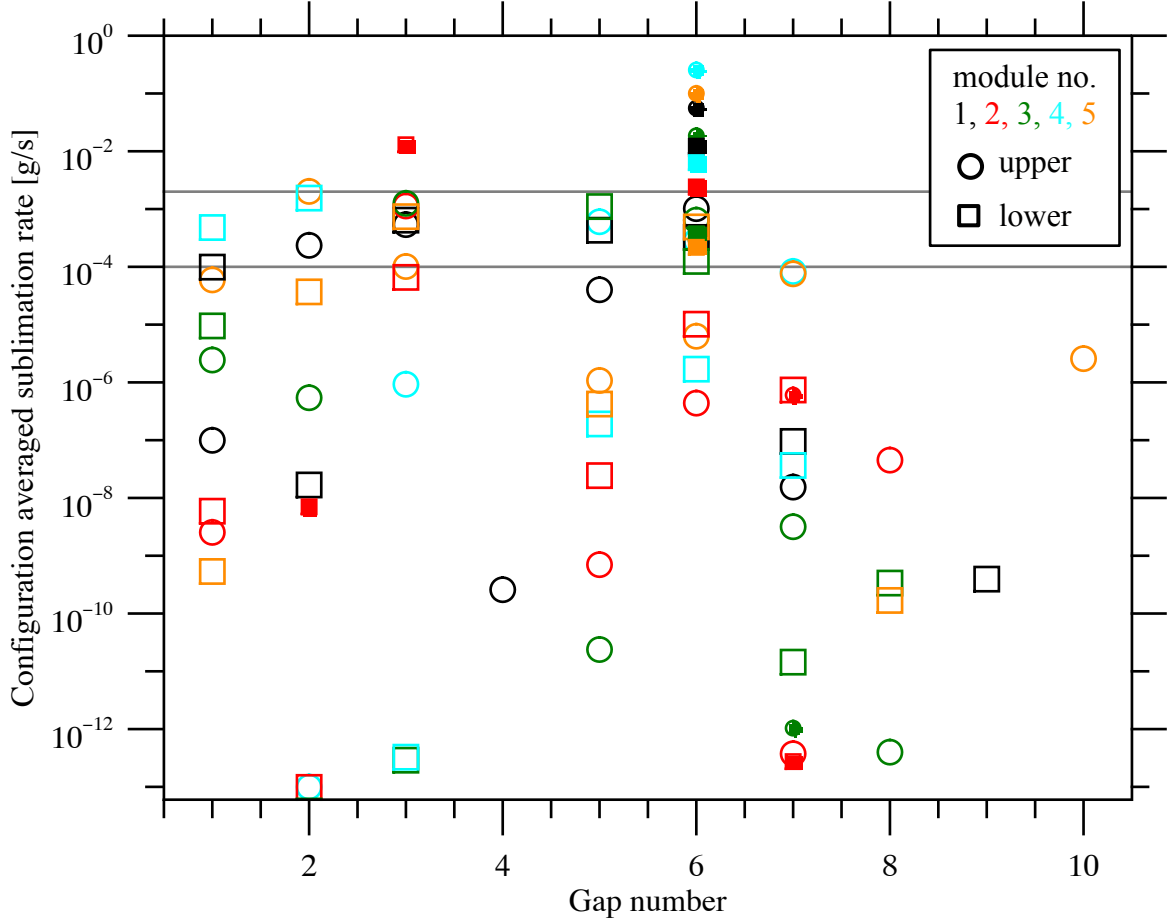
Figure 12: *Carbon sublimation rates $e_{tot}(t = 8\,s)$ for $10\,MW$ heating power, weighted average for magnetic configurations relevant for the TDU operation phase, as calculated in our model, for the step heights measured after the integration of the test divertor units into W7-X. The gaps are numbered in toroidal order for the horizontal target modules — 1: 1h-2h; 2: 2h, target elements (TE) 5-6; 3: 2h, TE 6-7; 4: 2h-3h; 5: 3h-4h; 6: 4h-5h1; 7: 5h1-5h2; 8: 5h2-6h2; 9: 7h-8h; 10: 8h-9h. Different colours for different machine modules, different symbols for upper and lower divertor units; full symbols: before re-alignment; open symbols: after re-alignment, or no re-alignment. Horizontal grey lines: indication of the thresholds $10^{-4}\,g/s$ and $2 \times 10^{-3}\,g/s$.*

the transport parallel to the magnetic field, the radial scale length of the SOL and hence the power density on the target plates, is simulated by the field line diffusion process with an empirical "diffusion coefficient" on the order of $1\,m^2/s$.

Within these limitations of our model, we find that the accuracy achieved in the

assembly of the W7-X TDU is in most locations sufficient to avoid an overheating of leading edges with significant carbon sublimation in discharges of up to $8\,\mathrm{s}$ with $10\,\mathrm{MW}$ of heating power, for those magnetic configurations envisaged for the TDU operation phase.

However, at the transition between the target modules 4h and 5h1, critical leading edges were found in several of the 10 divertor units. It was possible to re-install the target modules of type 5h1, using modified attachment brackets. The new measurements of the resulting step height showed that an alignment within $0.3\,\mathrm{mm}$ of the newly specified position could thus be achieved, in most cases even within $0.1\,\mathrm{mm}$. Without this re-alignment, significant carbon sublimation at these locations might have resulted for several magnetic configurations of interest.

According to our analysis of the as-built and re-aligned state of the W7-X test divertor, we do not expect operational limitations due to overheating of leading edges for the TDU operation phase.

Appendix: Thermal FEM Model

The temperature profiles of a graphite TE of $29\,\mathrm{mm}$ thickness with a leading edge have been calculated using a 2D FEM model in Abaqus 6.14-1 [18]. The automatically generated mesh was refined toward the leading edge with a minimum element size of $0.02\,\mathrm{mm}$. It contains $11\,907$ nodes and $11\,815$ first order iso-parametric solid 2D elements of type DC2D4 (quadrilateral) and DC2D3 (triangle). In fig. 13, we show the mesh and an exemplary temperature distribution. The thermal conductivity and heat capacity of the fine grain graphite Sigrafine$^{\circledR}$ R6510 of SGL was defined between $20°\,\mathrm{C}$ and $1\,600°\,\mathrm{C}$ based on data measured at Linseis GmbH by laser flash technique [19], see Figure 14. It was assumed that these values remain constant above $1\,600°\,\mathrm{C}$. An initial temperature of $20°\,\mathrm{C}$ was defined for all nodes.

To simulate the power density consumed per surface area by graphite sublimation q_{subl}, a convective boundary condition was applied along the red line in the left picture of fig. 13, with a sublimation film coefficient α_{subl} depending on the surface temperature, calculated as

$$\alpha_{\mathrm{subl}} = \frac{W\,e(T)}{T - T_{\mathrm{amb1}}} \tag{3}$$

with W and $e(T)$ from eq. (1) and an ambient temperature $T_{\mathrm{amb1}} = 0°\,\mathrm{C}$. In addition, a radiation boundary condition was defined along the surface exposed to the plasma, i.e.

$$q_{\mathrm{amb}} = \varepsilon\,\sigma\left(T^4 - T_{\mathrm{amb2}}{}^4\right), \tag{4}$$

assuming an ambient temperature T_{amb2} of $200°\,\mathrm{C}$ and an emissivity ε of 0.9.
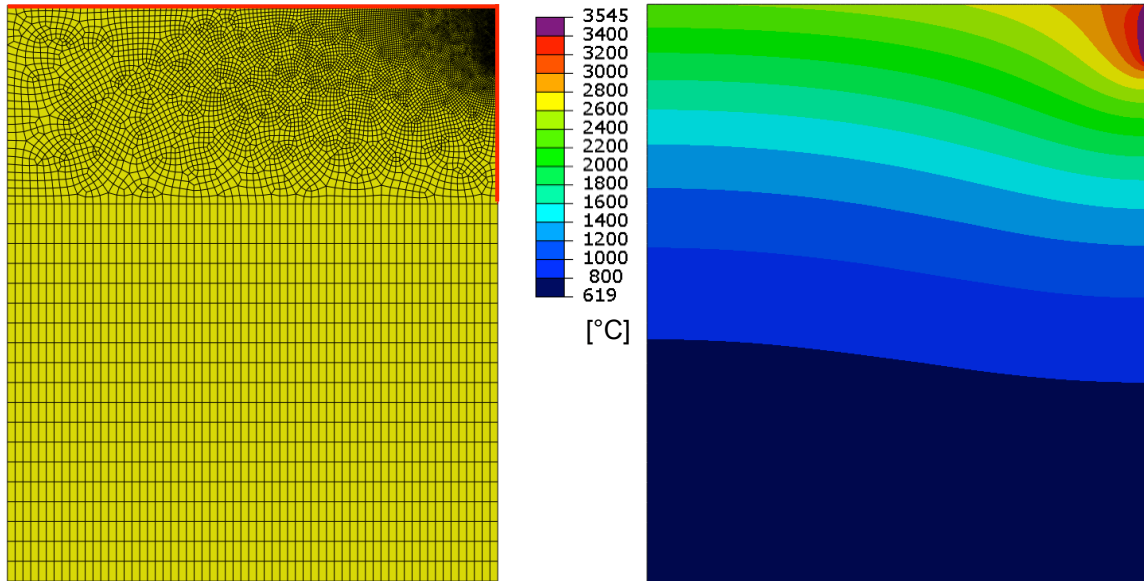
19

Figure 13: Mesh of the thermal model (left) and temperature distribution within a TE with a leading edge of 3 mm, exposed for 8 s to an incident heat flux of 230 MW/m² (right). The cross-section corresponds to the yz plane of fig. 4. Here, the y and z coordinates have different scales.
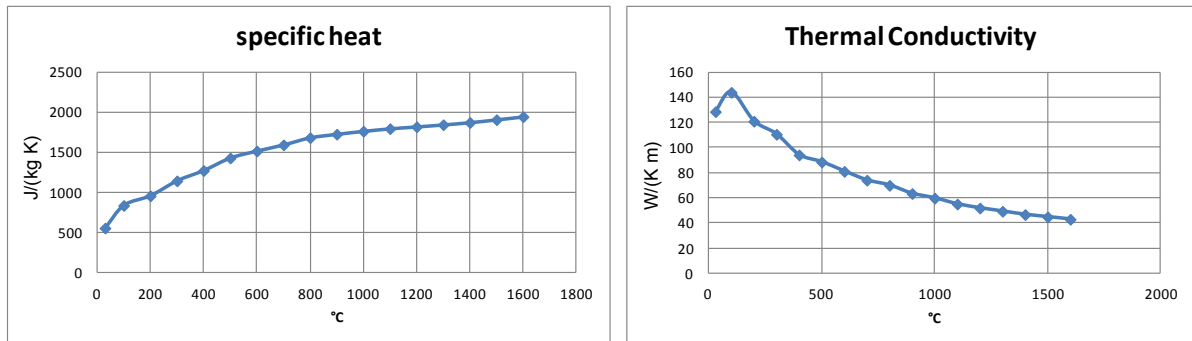

Figure 14: Thermal properties of graphite R6510 obtained in a laser flash test.

Transient thermal simulations were carried out for 40 seconds for 23×13 different cases: 23 different heights of the leading edge and 13 different values for the heat load to the leading edge, see table 1. A fixed ratio between the heat load onto the horizontal and vertical surface of 1:23 was chosen, corresponding to an incident angle of 2.5° of the magnetic field to the top surface of the TE. For each run, the temperatures along the red line of fig. 13 were extracted at fixed time points (see table 1) and stored in a table, to be used for further interpolation as discussed in section 4.1.

20

h_{LE} [mm]	0.04, 0.07, 0.1, 0.15, 0.2, 0.3, 0.4, 0.5, 0.6, 0.7, 0.8, 0.9, 1.0, 1.2, 1.4, 1.6, 1.8, 2.0, 2.2, 2.4, 2.6, 2.8, 3.0
P [MW/m^2]	10, 20, 30, 50, 70, 90, 110, 130, 150, 170, 190, 210, 230
time points t [s]	0, 0.1, 0.2, 0.3, 0.4, 0.5, 0.6, 0.8, 1.0, 1.5, 2, 3, 4, 5, 6, 7, 8, 9, 10, 15, 20, 30, 40

Table 1: Chosen values for the height of the leading edge h_{LE}, heat load to the leading edge P, and time points t after start of heat load.

Acknowledgements

References

[1] G. Grieger, C. Beidler, E. Harmeyer, W. Lotz, J. Kißlinger, P. Merkel, J. Nührenberg, F. Rau, E. Strumberger, and H. Wobig. Modular stellarator reactors and plans for WENDELSTEIN 7-X. *Fusion Technology*, **21**(3P2B) 1767–1778, May 1992.

[2] H.-S. Bosch et al. Technical challenges in the construction of the steady-state stellarator Wendelstein 7-X. *Nuclear Fusion*, **53**(12) 126001, December 2013.

[3] R. C. Wolf et al. Major results from the first plasma campaign of the Wendelstein 7-X stellarator. *Nuclear Fusion*, **57**(10) 102020, October 2017.

[4] T. Klinger, A. Alonso, S. Bozhenkov, R. Burhenn, A. Dinklage, G. Fuchert, J. Geiger, O. Grulke, A. Langenberg, M. Hirsch, G. Kocsis, J. Knauer, A. Krämer-Flecken,

H. Laqua, S. Lazerson, M. Landreman, H. Maaßberg, S. Marsen, M. Otte, N. Pablant, E. Pasch, K. Rahbarnia, T. Stange, T. Szepesi, H. Thomsen, P. Traverso, J. L. Velasco, T. Wauters, G. Weir, T. Windisch, and The Wendelstein 7-X Team. Performance and properties of the first plasmas of Wendelstein 7-X. *Plasma Phys. Contr. Fusion*, **59**(1) 014018, January 2017.

[5] Thomas Sunn Pedersen, Andreas Dinklage, Yuriy Turkin, Robert Wolf, Sergey Bozhenkov, Joachim Geiger, Golo Fuchert, Hans-Stephan Bosch, Kian Rahbarnia, Henning Thomsen, Ulrich Neuner, Thomas Klinger, Andreas Langenberg, Humberto Trimiño Mora, Petra Kornejew, Jens Knauer, Matthias Hirsch, W7-X Team, and Novimir Pablant. Key results from the first plasma operation phase and outlook for future performance in Wendelstein 7-X. *Phys. Plasmas*, **24**(5) 055503, May 2017.

[6] A. Peacock, H. Greuner, F. Hurd, J. Kißlinger, R. König, B. Mendelevitch, R. Stadler, F. Schauer, R. Tivey, J. Tretter, C. von Sehren, and M. Ye. Progress in the design and development of a test divertor (TDU) for the start of W7-X operation. *Fusion Engineering and Design*, **84**(7–11) 1475–1478, June 2009. Proceedings of the 25th Symposium on Fusion Technology (SOFT-25), Rostock, Germany, 15–19 September 2008.

[7] J. Boscary, A. Peacock, R. Stadler, B. Mendelevitch, H. Tittes, J. Tretter, M. Smirnow, and C. Li. Actively water-cooled plasma facing components of the Wendelstein 7-X stellarator. *Fusion Sci. Tech.*, **64**(2) 263–268, August 2013. Proceedings of the Twentieth Topical Meeting on the Technology of Fusion Energy (TOFE-2012) (Part 1), Nashville, Tennessee, August 27–31, 2012.

[8] H. Renner, J. Boscary, V. Erckmann, H. Greuner, H. Grote, J. Sapper, E. Speth, F. Wesner, M. Wanner, and W7-X Team. The capabilities of steady state operation at the stellarator W7-X with emphasis on divertor design. *Nuclear Fusion*, **40**(6) 1083–1093, June 2000.

[9] Y. Feng, C. D. Beidler, J. Geiger, P. Helander, H. Hölbe, H. Maassberg, Y. Turkin, D. Reiter, and W7-X Team. On the W7-X divertor performance under detached conditions. *Nuclear Fusion*, **56**(12) 126011, December 2016. http://stacks.iop.org/NF/56/126011.

[10] P. Sinha, H. Hölbe, T. S. Pedersen, S. Bozhenkov, and W7-X Team. Numerical studies of scrape-off layer connection length in Wendelstein 7-X. *Nuclear Fusion*, **58**(1) 016027, January 2018.

[11] S. A. Bozhenkov, J. Geiger, M. Grahl, J. Kißlinger, A. Werner, and R. C. Wolf. Service oriented architecture for scientific analysis at W7-X. An example of a field line tracer. *Fusion Engineering and Design*, **88**(11) 2997–3006, November 2013.

[12] V. Philipps, U. Samm, M. Z. Tokar', B. Unterberg, A. Pospieszczyk, and B. Schweer. Evidence of hot spot formation on carbon limiters due to thermal electron emission. *Nuclear Fusion*, **33**(6) 953–961, June 1993.

[13] Howard B. Palmer and Mordecai Shelef. Vaporization of carbon. In P. L. Walker, editor, *Chemistry and Physics of Carbon*, volume 4, pages 85–135. Dekker, New York, 1968.

[14] Y. Feng, F. Sardei, J. Kisslinger, P. Grigull, K. McCormick, and D. Reiter. 3D edge modeling and island divertor physics. *Contrib. Plasma Phys.*, **44**(1–3) 57–69, April 2004. Special Issue: Proceedings of 9th Workshop on Plasma Edge Theory in Fusion Devices (PET-9), September 3–5, 2003, University of California in San Diego, USA.

[15] H. Hölbe, T. Sunn Pedersen, J. Geiger, S. Bozhenkov, R. König, Y. Feng, J. Lore, A. Lumsdaine, and Wendelstein 7-X Team. Access to edge scenarios for testing a scraper element in early operation phases of Wendelstein 7-X. *Nuclear Fusion*, **56**(2) 026015, February 2016.

[16] J. Kisslinger, C. Beidler, E. Harmeyer, F. Rau, and H. Wobig. Magnetic field and coil systems of the modular Helias configuration HS 5-10. In B. E. Keen, M. Huguet, and R. Hemsworth, editors, *Fusion Technology 1990*, pages 1520–1524. Elsevier Science Publishers B. V., 1991. Proceedings of the 16th Symposium on Fusion Technology, London, U. K., 3–7 September 1990.

[17] S. P. Hirshman and W. I. van Rij. Three-dimensional free boundary calculations using a spectral Green's function method. *Computer Physics Communications*, **43**(1) 143–155, December 1986.

[18] 3DS Simulia Abaqus 6.14 Documentation Collection. Software Documentation, 2014. Dassault Systèmes, Vélizy-Villacoublay, France.

[19] J. Frohring. Linseis Application Laboratory Thermal Analysis, Sample Extracted from TDU-SE Graphite. Technical report, Linseis GmbH, Selb, Germany/Robbinsville, NJ, 22 June 2017. W7-X document no. 1-GXB-T0023.0.